1-1-2013

# Improving the depth sensitivity of time-resolved measurements by extracting the distribution of times-of-flight

Mamadou Diop
*Lawson Health Research Institute*

Keith St. Lawrence
*Lawson Health Research Institute*, kstlawr@uwo.ca

Citation of this paper:
Diop, Mamadou and St. Lawrence, Keith, "Improving the depth sensitivity of time-resolved measurements by extracting the distribution of times-of-flight" (2013). *Paediatrics Publications*. 2061.
https://ir.lib.uwo.ca/paedpub/2061

Biomedical Optics EXPRESS

# Improving the depth sensitivity of time-resolved measurements by extracting the distribution of times-of-flight

**Mamadou Diop**[1,2,*] **and Keith St. Lawrence**[1,2]

[1]*Imaging Program, Lawson Health Research Institute, London, Ontario N6A 4V2, Canada*
[2]*Department of Medical Biophysics, Western University, London, Ontario N6A 3K7, Canada*
**mdiop@lawsonimaging.ca*

**Abstract:** Time-resolved (TR) techniques provide a means of discriminating photons based on their time-of-flight. Since early arriving photons have a lower probability of probing deeper tissue than photons with long time-of-flight, time-windowing has been suggested as a method for improving depth sensitivity. However, TR measurements also contain instrument contributions (instrument-response-function, IRF), which cause temporal broadening of the measured temporal point-spread function (TPSF) compared to the true distribution of times-of-flight (DTOF). The purpose of this study was to investigate the influence of the IRF on the depth sensitivity of TR measurements. TPSFs were acquired on homogeneous and two-layer tissue-mimicking phantoms with varying optical properties. The measured IRF and TPSFs were deconvolved using a stable algorithm to recover the DTOFs. The microscopic Beer-Lambert law was applied to the TPSFs and DTOFs to obtain depth-resolved absorption changes. In contrast to the DTOF, the latest part of the TPSF was not the most sensitive to absorption changes in the lower layer, which was confirmed by computer simulations. The improved depth sensitivity of the DTOF was illustrated in a pig model of the adult human head. Specifically, it was shown that dynamic absorption changes obtained from the late part of the DTOFs recovered from TPSFs acquired by probes positioned on the scalp were similar to absorption changes measured directly on the brain. These results collectively demonstrate that this method improves the depth sensitivity of TR measurements by removing the effects of the IRF.

**OCIS codes:** (170.3660) Light propagation in tissues; (170.3890) Medical optics instrumentation.

## References and links

1. F. F. Jöbsis, “Noninvasive, infrared monitoring of cerebral and myocardial oxygen sufficiency and circulatory parameters,” Science **198**(4323), 1264–1267 (1977).
2. C. Dani, S. Pratesi, G. Fontanelli, J. Barp, and G. Bertini, “Blood transfusions increase cerebral, splanchnic, and renal oxygenation in anemic preterm infants,” Transfusion **50**(6), 1220–1226 (2010).
3. M. Diop, J. T. Elliott, K. M. Tichauer, T.-Y. Lee, and K. St. Lawrence, “A broadband continuous-wave multichannel near-infrared system for measuring regional cerebral blood flow and oxygen consumption in newborn piglets,” Rev. Sci. Instrum. **80**(5), 054302 (2009).
4. H. W. Schytz, T. Wienecke, L. T. Jensen, J. Selb, D. A. Boas, and M. Ashina, “Changes in cerebral blood flow after acetazolamide: an experimental study comparing near-infrared spectroscopy and SPECT,” Eur. J. Neurol. **16**(4), 461–467 (2009).
5. M. Belau, M. Ninck, G. Hering, L. Spinelli, D. Contini, A. Torricelli, and T. Gisler, “Noninvasive observation of skeletal muscle contraction using near-infrared time-resolved reflectance and diffusing-wave spectroscopy,” J. Biomed. Opt. **15**(5), 057007 (2010).
6. D. W. Brown, J. Hadway, and T.-Y. Lee, “Near-infrared spectroscopy measurement of oxygen extraction fraction and cerebral metabolic rate of oxygen in newborn piglets,” Pediatr. Res. **54**(6), 861–867 (2003).

#179884 - $15.00 USD Received 13 Nov 2012; revised 24 Jan 2013; accepted 13 Feb 2013; published 15 Feb 2013

7. D. A. Boas, T. Gaudette, G. Strangman, X. Cheng, J. J. Marota, and J. B. Mandeville, “The accuracy of near infrared spectroscopy and imaging during focal changes in cerebral hemodynamics,” Neuroimage **13**(1), 76–90 (2001).
8. A. Liebert, H. Wabnitz, J. Steinbrink, H. Obrig, M. Möller, R. Macdonald, A. Villringer, and H. Rinneberg, “Time-resolved multidistance near-infrared spectroscopy of the adult head: intracerebral and extracerebral absorption changes from moments of distribution of times of flight of photons,” Appl. Opt. **43**(15), 3037–3047 (2004).
9. L. Gagnon, C. Gauthier, R. D. Hoge, F. Lesage, J. Selb, and D. A. Boas, “Double-layer estimation of intra- and extracerebral hemoglobin concentration with a time-resolved system,” J. Biomed. Opt. **13**(5), 054019 (2008).
10. J. Steinbrink, H. Wabnitz, H. Obrig, A. Villringer, and H. Rinneberg, “Determining changes in NIR absorption using a layered model of the human head,” Phys. Med. Biol. **46**(3), 879–896 (2001).
11. J. T. Elliott, M. Diop, K. M. Tichauer, T.-Y. Lee, and K. St. Lawrence, “Quantitative measurement of cerebral blood flow in a juvenile porcine model by depth-resolved near-infrared spectroscopy,” J. Biomed. Opt. **15**(3), 037014 (2010).
12. D. T. Delpy, M. Cope, P. van der Zee, S. Arridge, S. Wray, and J. Wyatt, “Estimation of optical pathlength through tissue from direct time of flight measurement,” Phys. Med. Biol. **33**(12), 1433–1442 (1988).
13. M. S. Patterson, B. Chance, and B. C. Wilson, “Time resolved reflectance and transmittance for the non-invasive measurement of tissue optical properties,” Appl. Opt. **28**(12), 2331–2336 (1989).
14. B. Montcel, R. Chabrier, and P. Poulet, “Detection of cortical activation with time-resolved diffuse optical methods,” Appl. Opt. **44**(10), 1942–1947 (2005).
15. A. Kienle, M. S. Patterson, N. Dögnitz, R. Bays, G. Wagnivres, and H. van den Bergh, “Noninvasive determination of the optical properties of two-layered turbid media,” Appl. Opt. **37**(4), 779–791 (1998).
16. J. Selb, J. J. Stott, M. A. Franceschini, A. G. Sorensen, and D. A. Boas, “Improved sensitivity to cerebral hemodynamics during brain activation with a time-gated optical system: analytical model and experimental validation,” J. Biomed. Opt. **10**(1), 011013 (2005).
17. B. Montcel, R. Chabrier, and P. Poulet, “Time-resolved absorption and hemoglobin concentration difference maps: a method to retrieve depth-related information on cerebral hemodynamics,” Opt. Express **14**(25), 12271–12287 (2006).
18. M. Hiraoka, M. Firbank, M. Essenpreis, M. Cope, S. R. Arridge, P. van der Zee, and D. T. Delpy, “A Monte Carlo investigation of optical pathlength in inhomogeneous tissue and its application to near-infrared spectroscopy,” Phys. Med. Biol. **38**(12), 1859–1876 (1993).
19. D. Contini, A. Torricelli, A. Pifferi, L. Spinelli, F. Paglia, and R. Cubeddu, “Multi-channel time-resolved system for functional near infrared spectroscopy,” Opt. Express **14**(12), 5418–5432 (2006).
20. A. Liebert, H. Wabnitz, D. Grosenick, and R. Macdonald, “Fiber dispersion in time domain measurements compromising the accuracy of determination of optical properties of strongly scattering media,” J. Biomed. Opt. **8**(3), 512–516 (2003).
21. P. C. Hansen, *Discrete Inverse Problems: Insight and Algorithms* (Society for Industrial and Applied Mathematics, 2010).
22. G. Bodi and Y. Bérubé-Lauzière, “A new deconvolution technique for time-domain signals in diffuse optical tomography without a priori information,” in *European Conference on Biomedical Optics (ECBO)*, R. Cubeddu, and A. Hielscher, eds. (Optical Society of America, Munich, Germany, 2009), p. 7369.
23. M. Diop and K. St. Lawrence, “Deconvolution method for recovering the photon time-of-flight distribution from time-resolved measurements,” Opt. Lett. **37**(12), 2358–2360 (2012).
24. M. Diop, K. M. Tichauer, J. T. Elliott, M. Migueis, T.-Y. Lee, and K. St. Lawrence, “Comparison of time-resolved and continuous-wave near-infrared techniques for measuring cerebral blood flow in piglets,” J. Biomed. Opt. **15**(5), 057004 (2010).
25. H. Dehghani, M. E. Eames, P. K. Yalavarthy, S. C. Davis, S. Srinivasan, C. M. Carpenter, B. W. Pogue, and K. D. Paulsen, “Near infrared optical tomography using NIRFAST: Algorithm for numerical model and image reconstruction,” Commun. Numer. Methods Eng. **25**(6), 711–732 (2009).
26. J. T. Elliott, D. Milej, A. Gerega, W. Weigl, M. Diop, L. B. Morrison, T.-Y. Lee, A. Liebert, and K. St. Lawrence, “Variance of time-of-flight distribution is sensitive to cerebral blood flow as demonstrated by ICG bolus-tracking measurements in adult pigs,” Biomed. Opt. Express **4**(2), 206–218 (2013).
27. A. Kienle and M. S. Patterson, “Improved solutions of the steady-state and the time-resolved diffusion equations for reflectance from a semi-infinite turbid medium,” J. Opt. Soc. Am. A **14**(1), 246–254 (1997).
28. M. Diop, K. M. Tichauer, J. T. Elliott, M. Migueis, T.-Y. Lee, and K. St. Lawrence, “Time-resolved near-infrared technique for bedside monitoring of absolute cerebral blood flow,” Proc. SPIE **7555**, 75550Z (2010).
29. V. Ntziachristos, X. Ma, A. G. Yodh, and B. Chance, “Multichannel photon counting instrument for spatially resolved near infrared spectroscopy,” Rev. Sci. Instrum. **70**(1), 193–201 (1999).
30. M. Mäkitalo and A. Foi, “Optimal inversion of the Anscombe transformation in low-count Poisson image denoising,” IEEE Trans. Image Process. **20**(1), 99–109 (2011).
31. P. C. Hansen, “Regularization Tools Version 4.0 for Matlab 7.3,” Numer. Algorithms **46**(2), 189–194 (2007).
32. V. Ntziachristos and B. Chance, “Accuracy limits in the determination of absolute optical properties using time-resolved NIR spectroscopy,” Med. Phys. **28**(6), 1115–1124 (2001).
33. L. Hervé, A. Puszka, A. Planat-Chrétien, and J. M. Dinten, “Time-domain diffuse optical tomography processing by using the Mellin-Laplace transform,” Appl. Opt. **51**(25), 5978–5988 (2012).

#179884 - $15.00 USD Received 13 Nov 2012; revised 24 Jan 2013; accepted 13 Feb 2013; published 15 Feb 2013

34. H. Wabnitz, A. Liebert, D. Contini, L. Spinelli, and A. Torricelli, "Depth selectivity in time-domain optical brain imaging based on time windows and moments of time-of-flight distributions," in *Biomedical Optics, OSA Technical Digest* (Optical Society of America, St. Petersburg, Florida, 2008), p. BMD9.
35. H. Wabnitz, A. Jelzow, M. Mazurenka, O. Steinkellner, R. Macdonald, A. Pifferi, A. Torricelli, D. Contini, L. Zucchelli, L. Spinelli, R. Cubeddu, D. Milej, N. Zolek, M. Kacprzak, A. Liebert, S. Magazov, J. Hebden, F. Martelli, P. Di Ninni, and G. Zaccanti, "Performance Assessment of Time-Domain Optical Brain Imagers: The nEUROPt Protocol," in *Biomedical Optics and 3D Imaging* (Miami, 2012).
36. M. Diop and K. St. Lawrence, "A deconvolution method for recovering tissue impulse response from time-resolved measurements," in *Biomedical Optics (BIOMED)* (Miami, 2012).
37. S. L. Davis, P. J. Fadel, J. Cui, G. D. Thomas, and C. G. Crandall, "Skin blood flow influences near-infrared spectroscopy-derived measurements of tissue oxygenation during heat stress," J. Appl. Physiol. **100**(1), 221–224 (2006).

## 1. Introduction

Light in the near-infrared range is weakly absorbed by biological tissue, which enables deeper lying organs such as the brain or muscle to be monitored by probes placed on the skin [1–5]. Furthermore, near-infrared spectroscopy (NIRS) provides a noninvasive approach for monitoring tissue function due to the unique absorption properties of oxygenated and deoxygenated haemoglobin [6]. Despite these advantages, the accuracy of NIRS, even when used for monitoring relative tissue oxygenation, is challenged by light absorption in superficial tissue [7–10]. Methods for separating the contributions from different tissue layers typically rely on multi-distance measurements, which take advantage of the increased depth penetration of photons detected at larger source–detector separations [11]. Multi-distance methods are, however, sensitive to the skin microvasculature under the probes, which can significantly affect the accuracy of the measurements [10]. An alternative approach is time-resolved (TR) NIRS, which involves injecting short light pulses, typically in the range of picoseconds, into a medium and measuring the temporal distribution of the diffusely reflected or transmitted light [12–14]. The distribution of times-of-flight (DTOF) of photons provides a means of separating absorption changes in different tissue layers since light travelling through superficial tissue is detected earlier than light that penetrates the deeper layers [15,16].

In addition, the linear relationship between optical pathlength and time-of-flight, in combination with the microscopic Beer-Lambert law (MBLL), provides a theoretical framework for determining changes in absorption coefficient ($\Delta\mu_a$) from TR data [17–19]. However, applying the MBLL may be confounded by the instrument response function (IRF), which causes temporal dispersion of the measured temporal point-spread function (TPSF) compared to the true DTOF [20]. Removing the effects of the IRF requires performing a deconvolution, which is known to be an ill-posed problem [21]. Thus, small perturbations in the measurements, such as due to Poisson noise inherent to photon detection, will result in large fluctuations in the recovered DTOF [22,23]. We have recently developed a stable deconvolution algorithm incorporating signal denoising and constrained regularization that is capable of recovering the DTOF from TR measurements (i.e., IRF and TPSF) [23].

In this article, the effects of the IRF on the ability to separate absorption changes in superficial and deep tissue layers were investigated. Time-resolved data were acquired from two tissue-mimicking phantoms (homogeneous and two-layered) with varying absorption coefficients. The MBLL was applied to the measured TPSFs and to the DTOFs retrieved by the deconvolution algorithm. The pathlength-resolved $\Delta\mu_a$ obtained from the two data sets were compared in order to assess the effects of the IRF on depth sensitivity. The experimental results were verified by applying the MBLL to simulated DTOFs and TPSFs obtained using the NIRFAST toolbox for geometries similar to the tissue-mimicking phantoms. Finally, the ability to obtain *in vivo* $\Delta\mu_a$ measurements from DTOFs was demonstrated by acquiring TR data from an animal model (pig) of the adult head. The absorption coefficient was changed by injecting indocyanine green (ICG), and measurements were acquired by probes positioned on the scalp and directly on the brain to investigate the depth sensitivity of the technique.

#179884 - $15.00 USD Received 13 Nov 2012; revised 24 Jan 2013; accepted 13 Feb 2013; published 15 Feb 2013

## 2. Materials and methods

### *2.1 Instrumentation*

The light source of the TR instrument was a picosecond pulsed diode laser emitting at 802 nm (LDH-P-C-810, PicoQuant, Germany). The laser output power and the pulse repetition rate were set to 1.4 mW and 80 MHz, respectively. The laser output was coupled by a microscope objective lens (N.A. = 0.25, magnification = 10X) into a 1.5 m long multimode fiber (N.A. = 0.22, core 400 µm; Fiberoptics Technology, Pomfret, CT). Two variable neutral density filters (NDC-50-4M, Thorlabs, Newton, NJ) placed between the laser head and the fiber were used to adjust the laser power delivered to the sample. Diffusely reflected light from the sample was collected by a 2-m fiber optic bundle (N.A. = 0.55, 3.6 mm active area; Fiberoptics Technology) whose distal end was secured in front of a Peltier-cooled photomultiplier tube (PMC-100, Becker & Hickl, Germany). Detection of a photon generated an electrical pulse that was transmitted to a time-correlated single photon counting (TCSPC) module (SPC-134, Becker & Hickl, Germany). Because the TCSPC module had a dead time of 100 ns, the count rate was adjusted to a typical rate of 800 kHz to minimize any dead-time effects. This count rate, which was 1% of the laser pulse repetition rate, also minimized pile-up effects [24].

The IRF was measured by placing a thin piece of white paper between the emission fiber and the detection probe. The paper was coated with black toner to reduce back-reflection from the emission fiber [24]. The IRF was acquired at a count rate of 800 kHz to match the baseline count rate used in the experiments.

### *2.2 Tissue-mimicking phantom experiments*

Experiments were conducted using a two-layer tissue-mimicking phantom consisting of a deep bottom layer (17.5 × 17.5 × 9.5 cm, L × W × H) and a removable shallow top layer (17.5 × 17.5 × 1.0 cm), each filled with a 0.7% intralipid solution (Fig. 1). The two layers were separated by a thin plastic film of a matte finish, which reduced specular reflection. Measurements were conducted as follows. First, the top layer was removed and the source and detector optodes were positioned on the surface of the bottom layer at an interoptode distance of 3 cm. Second, the laser power was adjusted to obtain a baseline count rate of 800 kHz and 32 TPSFs were acquired from the homogeneous medium. Next, the top layer was repositioned and 32 TPSFs were acquired with the optodes placed on its surface as shown in Fig. 1. This procedure was repeated five times. Each step involved adding 1 ml of an india ink solution (0.5 mL of stock ink in 10 mL of 0.7% intralipid) to the bottom layer to change its absorption coefficient and acquiring measurements for both the homogeneous and two-layer conditions. Note that the optical properties of the top layer remained the same throughout the experiment, and each TPSF was acquired with an integration time of 1s.

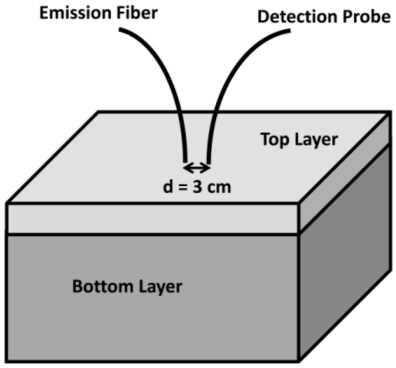

Fig. 1. Schematic of the two-layer phantom. Measurements for a homogeneous medium were acquired by removing the top layer and placing the emission and detection optodes 3 cm apart on the surface of the bottom layer.

#179884 - $15.00 USD Received 13 Nov 2012; revised 24 Jan 2013; accepted 13 Feb 2013; published 15 Feb 2013

### *2.3 Forward model simulations*

To verify the experimental phantom measurements, simulated time-resolved data for homogeneous and two-layer media with varying absorption properties were generated using the NIRFAST toolbox [25]. NIRFAST is based on the finite element method (FEM) and provides the ability to model near-infrared light propagation in tissue with complex geometries (more details about NIRFAST can be found in [25]). The size of the simulated homogeneous medium was 10 × 10 × 9 cm (L × W × H) with a node distance of 0.2 cm. For the simulated two-layer case, the dimensions of the bottom and top layers were 10 × 10 × 8 cm and 10 × 10 × 1 cm, respectively, with the same node distance as for the homogeneous case. The initial absorption and scattering coefficients were set to 0.029 and 7.2 $\text{cm}^{-1}$, respectively, in both cases. The values of the absorption coefficient ($\mu_a$) of the homogeneous medium and the bottom part of the two-layer medium were varied from 0.029 to 0.085 $\text{cm}^{-1}$ in steps of 0.014 $\text{cm}^{-1}$, while their reduced scattering coefficient ($\mu_s'$) and both optical properties of the top layer were kept constant. These values were chosen to match the optical properties of the tissue-mimicking phantoms. For each set of optical properties, a DTOF was simulated and analyzed by the MBLL to extract pathlength-resolved absorption changes. To mimic typical experimental measurements, the simulated DTOFs were convolved with the measured IRF to generate theoretical TPSFs, which were also analyzed with the MBLL.

### *2.4 Animal experiment*

A female pig weighting 15 kg was delivered the morning of the experiment from a local farm. The animal was anesthetized with 1.75% isofluorane (3% during surgery), tracheotomized and mechanically ventilated on an oxygen/medical air mixture. A femoral artery was catheterized to monitor heart rate and blood pressure, and to collect blood gas samples. Body temperature was maintained between 37.5 and 38.5°C. Blood glucose, anesthetic level and respiration rate were monitored and adjusted, when necessary, to maintain constant physiological parameters throughout the experiment. After surgery, the animal was placed in the prone position and allowed to stabilize for 1 hour before any measurement was acquired. The experiment was approved by the Animal Use Subcommittee of Western University and followed the guidelines of the Canadian Council on Animal Care.

A custom-made probe holder, which housed the emission and detection optodes of the TR system, was positioned on the pig head and fixed in place with tissue glue. Measurements were acquired on the scalp and directly on the brain. For the scalp measurements, three incisions were made around the probe holder to reduce scalp blood flow [26]. Two series of TPSFs were acquired at an integration time of 0.4 s for 5 min, each following a rapid intravenous injection of an ICG bolus (0.1 mg/kg, Sigma-Aldrich, St. Louis, MO). Following these measurements, the scalp under the probe holder was removed and two holes were drilled through the skull at the probe positions. The probes were inserted into the holes until they rested on the dura matter and a second series of TPSFs was acquired following another iv ICG injection.

## 3. Data analysis

### *3.1 Quantification of the optical properties of the phantom*

The optical properties (i.e., $\mu_a$ and $\mu_s'$) of the homogeneous phantom were determined using the solution to the diffusion equation for a homogeneous semi-infinite medium [27]. The model solution was first convolved with the measured IRF, and then a nonlinear optimization routine (MATLAB function fminsearch) was used to fit the convolved model to each measured TPSF. The fitting range was set to 80% of the peak value on the leading edge and 20% on the falling edge [28].

#179884 - $15.00 USD Received 13 Nov 2012; revised 24 Jan 2013; accepted 13 Feb 2013; published 15 Feb 2013

### *3.2 Deconvolution*

A measured TPSF can be expressed as a convolution between the IRF and the true DTOF [23,29]:

$$TPSF = IRF * DTOF \tag{1}$$

where * denotes the convolution operator. Recovering the DTOF from Eq. (1) was performed using a two-stage deconvolution technique based on signal denoising and two-stage Tikhonov regularization [30,31]. The first stage uses a standard Tikhonov regularization to recover the general shape of the DTOF, and the second stage involves an adaptive weighting algorithm designed to stabilize the final DTOF.

For the deconvolution, Eq. (1) is re-written in a discrete integral form:

$$TPSF(m\Delta t) = \sum_{n=0}^{m-1} IRF([m-n]\Delta t) DTOF(n\Delta t)\Delta t \tag{2}$$

where $\Delta t$ refers to the sampling interval. To improve the stability of the solution, a regularization condition is added to Eq. (2) to obtain:

$$\min_x (\|Ax - b\|_2^2 + \lambda^2 \|WLx\|_2^2) \tag{3}$$

The second term in Eq. (3) provides a smoothness constraint whose weight is controlled by the Lagrange multiplier ($\lambda$). $L$ is the $M \times M$ second-derivative operator matrix, and $W$ is an additional $M \times M$ weighting matrix.

In the first stage of the deconvolution, Eq. (3) is solved using an unweighted second-derivative operator (i.e., $W$ is set to the identity matrix). The derived DTOF, which typically contains unwanted oscillations due to noise in the original TR data, is used to guide the selection of the values of $W$ in the second stage of the deconvolution. Specifically, the values of the elements of $W$ are chosen to slowly increase the weight of the smoothness from the initial rise to the tail of the DTOF curve. In addition, the weighting of the last 20% on the tail (relative to the maximum of the DTOF) is multiplied by a coefficient ($\alpha$) to further stabilize the solution. The optimal $\alpha$ value is selected by plotting the ratio of the weighted smoothness norm to the residue norm over a range of coefficients (e.g., $10^{-3}$ to $10^{3}$), and choosing the value that corresponds to the rise of the resulting L-shaped curve [23]. Note that the weighting coefficients do not depend on the optical properties but on the signal-to-noise-ratio of the data. An additional non-negative constraint is also imposed to the initial part of the curve to further stabilize the solution. During both stages, Eq. (3) is solved using the generalized singular value decomposition of the matrix pair ($A$, $WL$) in combination with the *L-curve* method [21].

### *3.3 Microscopic Beer-Lambert law*

An absorption change ($\Delta\mu_{a,i}$) will induce a change in the number of detected photons along the $i^{th}$ pathlength ($L_i$), which can be expressed as [10,32]:

$$-\ln\left(\frac{N_i(T)}{N_i(0)}\right) = \Delta\mu_{a,i} L_i \tag{4}$$

where $N_i(0)$ and $N_i(T)$ are the number of detected photons before and after an absorption change. The primary difficulty when applying Eq. (4) to TR NIRS measurements is the evaluation of $L_i$ since the IRF increased the total width of the TPSF. However, if the effects of the IRF on the TR data are removed by deconvolution, a pathlength can be recast in terms of the true time-of-flight:

#179884 - $15.00 USD Received 13 Nov 2012; revised 24 Jan 2013; accepted 13 Feb 2013; published 15 Feb 2013

$$-\ln\left(\frac{N_i(T)}{N_i(0)}\right)=\Delta\mu_{a,i}vt_i \quad (5)$$

where $v$ is the speed of light in the medium (assuming a tissue refractive index of 1.4) and $t_i$ is the time-of-flight of the detected photons along the path $L_i$. Equation (5) is known as the microscopic Beer-Lambert law and was used to calculate $\Delta\mu_a$ for a range of pathlengths (Figs. 2 and 3) or for specific pathlengths (Fig. 4).

## 4. Results

Figure 2(a) shows the TPSFs measured on the homogeneous phantom at the five $\mu_a$ values (Table 1). The curves in Fig. 2(b) are the corresponding DTOFs obtained by deconvolution. The pathlength scale in Fig. 2(a) is greater than in Fig. 2(b) because the TPSFs are the convolution of the IRF and the DTOFs. The pathlength-resolved absorption changes ($\Delta\mu_a$) recovered from the homogeneous phantom data, using the raw TPSFs in Fig. 2(a) and the deconvolved DTOFs in Fig. 2(b), are displayed in Figs. 2(c) and 2(d), respectively. For comparison, Figs. 2(e) and 2(f) show the pathlength-resolved $\Delta\mu_a$ recovered from the simulated TPSFs and DTOFs, respectively. For a homogeneous medium, $\Delta\mu_a$ should be independent of pathlength as shown in Fig. 2(f). Therefore, the dependency of $\Delta\mu_a$ on pathlength observed in both the experimental and simulated TPSF data (Figs. 2(c) and 2(e)) is clearly an artefact of the temporal blurring caused by the IRF. Unlike the TPSF results, the data derived from the DTOFs data exhibited no pathlength dependency (Figs. 2(d) and 2(f)).

Table 1 displays the $\mu_a$ and $\mu_s'$ values recovered by fitting the TPSFs in Fig. 2(a) using the procedure describe in section 3.1. The optical properties of the top layer were kept unaltered during the entire experiment. The intralipid solution used to fill the top layer was taken from the same 0.7% intralipid solution used as the baseline solution for the homogeneous phantom. Consequently, the $\mu_a$ and $\mu_s'$ values of the top layer were 0.029 $\text{cm}^{-1}$ and 7.1 $\text{cm}^{-1}$, respectively.

**Table 1. Optical properties of the bottom layer (i.e. the homogeneous phantom)[a]**

| Condition | $\mu_a$ ($\text{cm}^{-1}$) | $\mu_s'$ ($\text{cm}^{-1}$) |
|---|---|---|
| Baseline | 0.029 | 7.1 |
| Step 1 | 0.043 | 7.2 |
| Step 2 | 0.057 | 7.3 |
| Step 3 | 0.071 | 7.3 |
| Step 4 | 0.084 | 7.3 |

[a] At each step, an additional 1 ml of an india ink solution was added to the bottom layer.

#179884 - $15.00 USD Received 13 Nov 2012; revised 24 Jan 2013; accepted 13 Feb 2013; published 15 Feb 2013

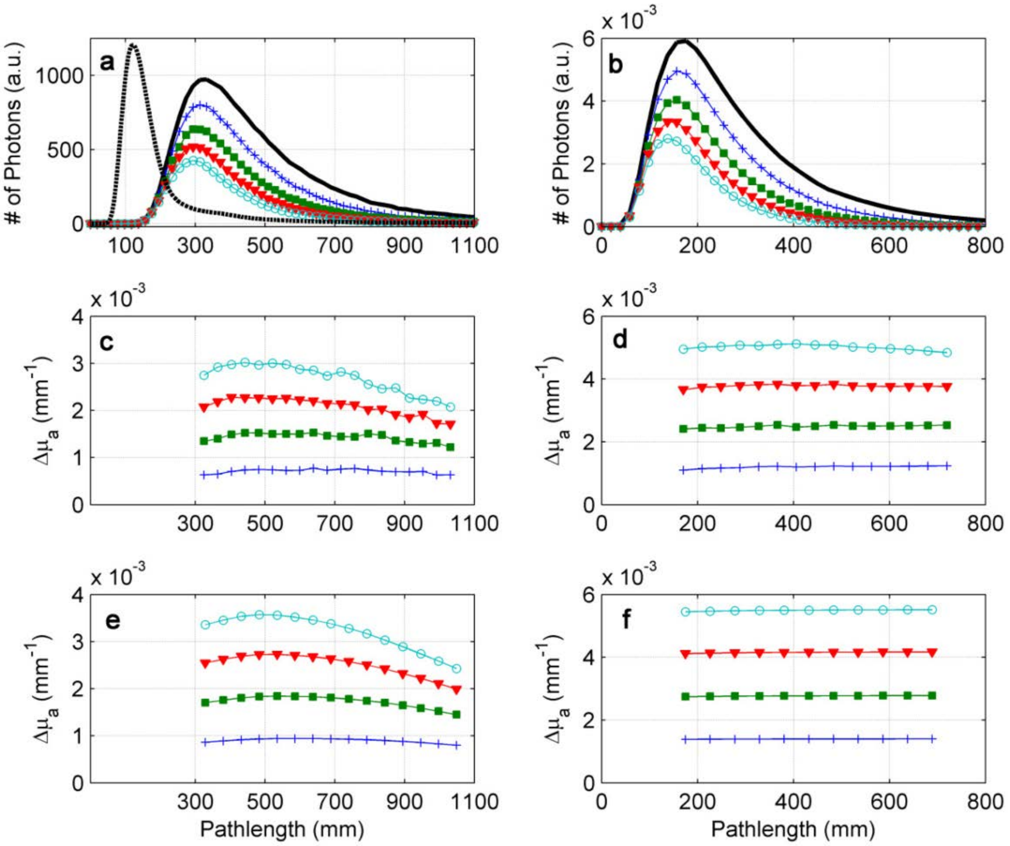

Fig. 2. (a) TPSFs measured with the emission and detection probes positioned 3 cm apart on the surface of the homogeneous phantom. The curves were obtained by averaging 32 individual TPSFs, each acquired for 1s. The solid black curve is the TPSF measured at baseline (acquired at 800 kHz) and the cyan curve with the open circles is the TPSF acquired at the highest absorption coefficient (step 4 in Table 1). The dashed black curve is the instrument response function (IRF). Note, the amplitude of the IRF was divided by three for visualization purpose. (b) Corresponding DTOFs obtained by deconvolving the IRF and TPSFs shown in (a). Pathlength-resolved absorption changes ($\Delta\mu_a$) recovered from the experimental TPSFs and the deconvolved DTOFs are shown in (c) and (d), respectively. The predicted $\Delta\mu_a$ from the simulated TPSFs and DTOFs are shown in (e) and (f), respectively.

Figure 3(a) shows the TPSFs measured on the two-layer phantom at each of the five $\mu_a$ values in the bottom layer. In all five conditions, the $\mu_a$ and $\mu_s'$ values of the top layer were kept constant. Similar to the homogenous phantom, each of the curves shown in Fig. 3(a) is the average of 32 individual TPSFs, and the corresponding DTOFs recovered from the two-stage deconvolution are shown in Fig. 3(b). In this case, the measured $\Delta\mu_a$ was expected to increase with pathlength since absorption was increased in the bottom layer. However, the pathlength-resolved $\Delta\mu_a$ recovered from the TPSFs data (Fig. 3(c)) did not display this expected behaviour, nor did the $\Delta\mu_a$ values obtained from the simulated TPSFs (Fig. 3(e)). In contrast the $\Delta\mu_a$ results obtained from the DTOFs exhibited the predicted increase with pathlength for both the experimental (Fig. 3(d)) and the simulated (Fig. 3(f)) data. The differences in the pathlength-resolved $\Delta\mu_a$ values derived from the TPSFs and the DTOFs are, again, a consequent of the confounding effects of the IRF. Note, the shift of the red curves with the triangles in Figs. 3(c) and 3(d) is due to errors caused by the difficulty of repositioning the probes between measurements.

#179884 - $15.00 USD Received 13 Nov 2012; revised 24 Jan 2013; accepted 13 Feb 2013; published 15 Feb 2013

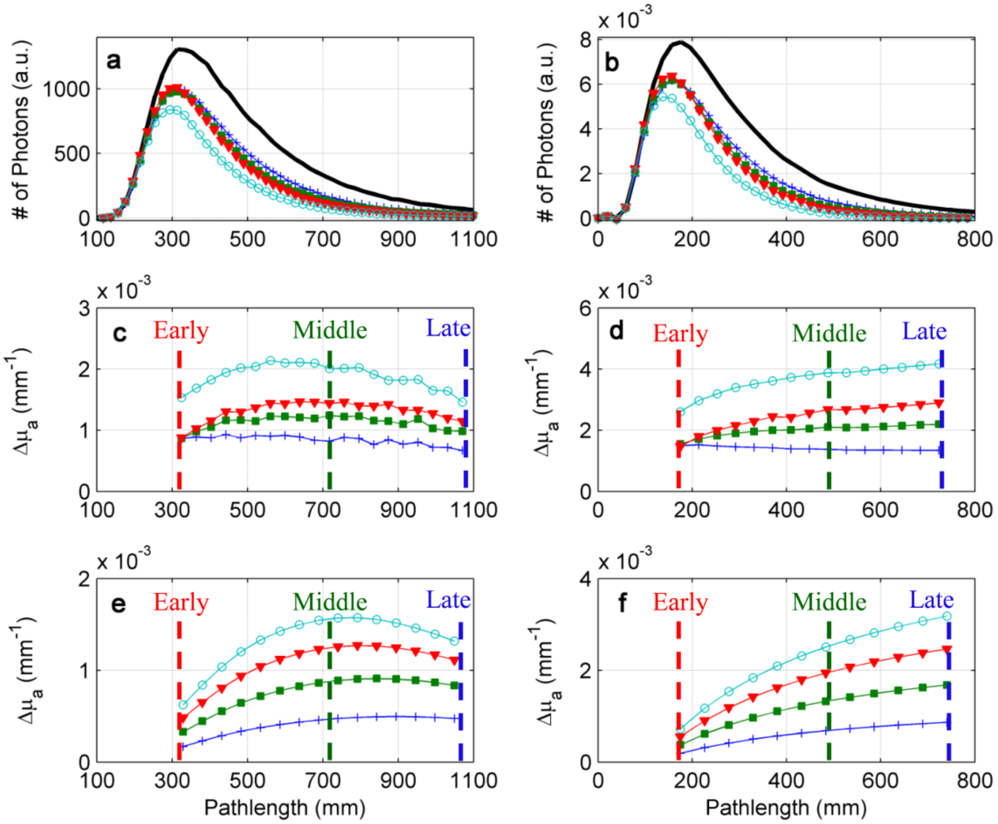

Fig. 3. (a) TPSFs measured with the probes positioned on the surface of the two-layer phantom. Each curve is the average of 32 TPSFs. The black curve is the TPSF at baseline and the cyan curve with the open circles is the TPSF acquired with the largest $\mu_a$ value in the bottom layer (step 4 in Table 1). (b) DTOFs obtained by deconvolving the IRF and TPSFs. Absorption changes ($\Delta\mu_a$) recovered from (c) the experimental TPSFs and (d) the corresponding DTOFs. Fig. (e) and (f) are the pathlength-resolved $\Delta\mu_a$ generated from (e) the simulated TPSFs and (f) the simulated DTOFs. The vertical dashed lines indicate the specific pathlengths used to obtain the data presented in Fig. 4.

Figure 4 displays the $\Delta\mu_a$ values recovered for the specific pathlengths indicated by the vertical dashed lines in Fig. 3. The early $\Delta\mu_a$ values correspond to a pathlength of 325 mm for the TPSF data and 174 mm for the DTOF data; the middle $\Delta\mu_a$ values correspond to pathlengths of 710 and 459 mm for the TPSF and DTOF data, respectively; and late $\Delta\mu_a$ values correspond to pathlengths of 1092 and 741 mm for the TPSF and DTOF data, respectively. The pathlength-specific $\Delta\mu_a$ values for the two-layer tissue-mimicking phantom are plotted against the $\Delta\mu_a$ values measured in the bottom layer of the phantom (Table 1). Similarly, the $\Delta\mu_a$ values recovered from the early, middle and late part of the TPSFs and DTOFs for the simulated two-layer medium are shown in Figs. 4(c) and 4(d), respectively. Note, the greater sensitivity of the middle time-window (green curves with the square symbols) to absorption changes in the bottom layer compared to the late time-window (blue curves with the triangles) for both the experimental (Fig. 4(a)) and theoretical (Fig. 4(c)) TPSFs data. In contrast, the late $\Delta\mu_a$ values from the DTOFs are higher than the middle $\Delta\mu_a$ values for both the experimental and simulated data. This further demonstrates the improved depth-sensitivity of the DTOFs compared to the TPSFs.

#179884 - $15.00 USD Received 13 Nov 2012; revised 24 Jan 2013; accepted 13 Feb 2013; published 15 Feb 2013

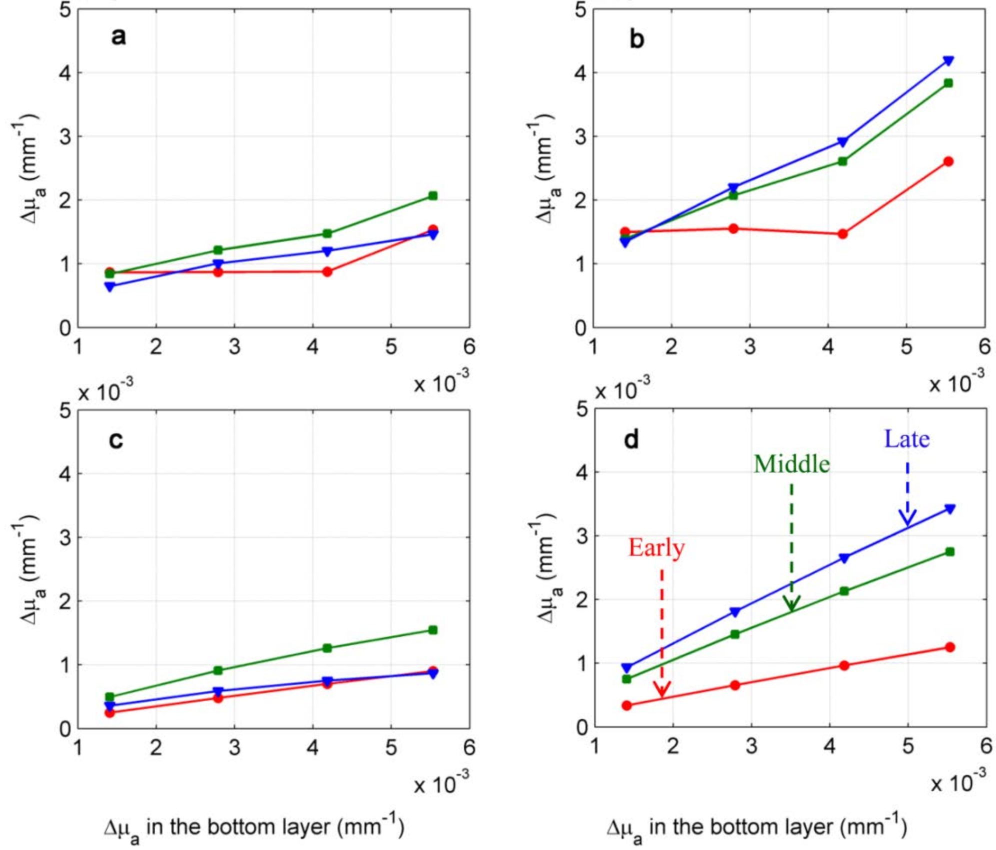

Fig. 4. The absorption changes ($\Delta\mu_a$) recovered from the two-layer media are plotted against $\Delta\mu_a$ in the bottom layer. The $\Delta\mu_a$ values are shown from early (red), middle (green) and late time-windows (blue) for experimental (a) TPSFs and (b) DTOFs, as well as for simulated (c) TPSFs and (d) DTOFs.

The time series of TPSFs acquired on the pig's head following ICG injections were deconvolved to extract sets of 100 DTOFs spanning 2.5 min. The time-varying change in absorption, $\Delta\mu_a$(t), determined from the recovered DTOFs is illustrated in Fig. 5. Specifically, Fig. 5(a) displays the normalized $\Delta\mu_a$(t) recovered from early (black; average time-of-flight ~0.5 ns) and late (blue curve with triangles: average time-of-flight ~1.4 ns) time-windows with the probes positioned on the scalp following an ICG injection. The width of the time-window was 0.1 ns. Figures 5(b) and 5(c) show the normalized absorption changes obtained when the probes were placed directly on the brain (red curve with the circles) and the $\Delta\mu_a$(t) recovered from the late time-window of the DTOFs when the probes were positioned on the scalp. Note, the blue curves in (a) and (b) are the same and the red curves in (b) and (c) are the same as well. The thickness of the extra-cerebral layers, measured by computed tomography, was 10.2 mm. The similarity between the $\Delta\mu_a$(t) recovered from the late time-window of the DTOFs when the probes were positioned on the scalp (blue and green curves in 5(b) and 5(c)) and $\Delta\mu_a$(t) measured directly on the brain (red curve in 5(b) and 5(c)), illustrates the sensitivity of the DTOFs to changes occurring in the brain.

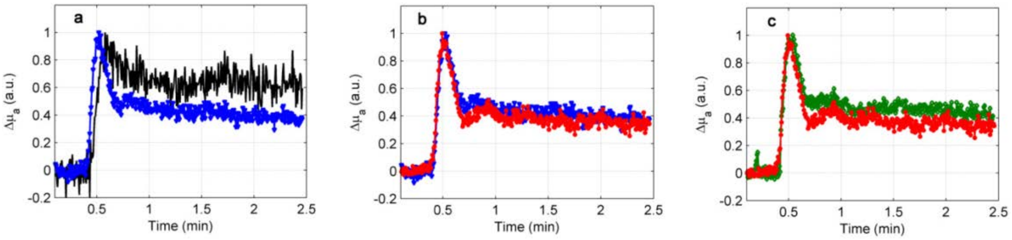

Fig. 5. (a) Normalized absorption changes for early (black) and late (blue) time-windows (width = 0.1 ns) obtained with the DTOFs recovered from the TPSFs measured by probes positioned on the pig's scalp at a source-detector separation of 3 cm. (b) and (c) Comparison of the normalized absorption changes determined with the probes placed directly on the brain (red curve with circles) and the normalized $\Delta\mu_a(t)$ obtained from late time-window of the DTOFs acquired with the probes on the scalp, following two distinct ICG injections (blue and green). Note that the red curves in (b) and (c) are the same.

## 5. Discussion

Time-resolved measurements (TPSFs) contain contributions of both the probed medium (i.e., the DTOF) and the instrument (i.e., the IRF), and the latter can cause significant temporal broadening of the measured TPSFs compared to the DTOFs. The effects of the IRF can be reduced by using TR instruments with narrower response functions, which can be achieved by using lasers with narrower pulse widths, less dispersive fibers (e.g., graded-index fibers) and single-photon detectors with narrow temporal responses. However, such instruments are more expensive and generally bulkier than the small footprint TR systems typically used for bedside monitoring, such as the one described in this study. Furthermore, it has been previously reported that the accuracy of recovering tissue optical properties from TR measurements is significantly deteriorated when the IRF is not taken into account in the fitting [20]. Consequently, when fitting methods are used to obtain tissue optical properties from TR measurements, the data are analyzed with a theoretical model convolved with the IRF, instead of a model alone [24,29]. However, a limitation with fitting methods is the difficulty of using a model for heterogeneous media. For example, in a two-layer medium, the thickness of the top layer is generally required in order to derive reasonably precise estimates of the optical properties [9].

Less restrictive depth-resolved alternatives, which also take into account the effects of the IRF, have been devised including moment-based analysis and a similar approach based on the Mellin-Laplace transform [8,33]. Moment analysis has been shown to be sensitive to depth-resolved trends in absorption changes, but it does not take full advantage of the rich information content of TR data since it typically provides at most three values (i.e., total number of photons, mean time-of-flight and variance) per TPSF. In addition, it has been shown that moment-based approaches are less sensitive to deep absorption changes than time-windowing [34]. In theory, time-windowing takes full advantage of the entire DTOF data set and can provide, as shown in this article, high resolution pathlength-resolved absorption changes from a single source-detector pair. Other advantages include the flexibility to vary the width and position of the time-windows and the applicability to any surface shapes [34].

Previous studies have alluded to the potential effects of the IRF on absorption changes recovered from TPSFs data when analyzed by the MBLL [10,17,35]. However, a rigorous investigation of how the IRF can potentially affect the absorption changes recovered from TR measurements has not been reported. The effects of the IRF can be substantial if its width is comparable to that of the DTOF, which is evident in Fig. 2. In these experiments, the IRF of the TR system had a full width at half maximum of 490 ps and also exhibited significant afterpulsing [28]. It is, therefore, not surprising that the late time-window of the measured TPSFs did not have the optimum depth sensitivity as these measurements will contain contributions from earlier arriving photons due to the temporal dispersion caused by the IRF.

#179884 - $15.00 USD Received 13 Nov 2012; revised 24 Jan 2013; accepted 13 Feb 2013; published 15 Feb 2013

In this study, these effects were demonstrated by recovering the true DTOFs using a recently developed algorithm that combines efficient signal denoising and a two-stage deconvolution method based on generalized singular value decomposition and Tikhonov regularization [23,36]. This algorithm recovers DTOFs with high fidelity, thereby enabling a direct comparison of absorption changes obtained from experimental TPSFs to those derived from the recovered DTOFs.

Absorption changes obtained from a homogeneous medium should not depend on pathlength, as confirmed by the $\Delta\mu_a$ values obtained from the DTOFs data (Fig. 2(d)). In contrast, the TPSFs results (Fig. 2(c)) exhibited a dependency of $\Delta\mu_a$ on pathlength. The unexpected decrease in $\Delta\mu_a$ with increasing pathlength is clearly an artefact caused by the IRF, as predicted by the results of the forward model simulations shown in Figs. 2(e) and 2(f). The consequence of this artefact could be an erroneous interpretation of TPSF-derived $\Delta\mu_a$ values. For example, the sample could be interpreted as a heterogeneous media due to the pathlength dependency of $\Delta\mu_a$. Furthermore in a two-layer medium, the measured $\Delta\mu_a$ is expected to increase with pathlength when absorption increases in the lower compartment. The DTOFs data (Figs. 3(d) and 3(f)) demonstrated the expected higher sensitivity of late-arriving photons to absorption changes in the bottom layer; while, the pathlength-resolved $\Delta\mu_a$ recovered from the raw TR data showed that the latest part of the TPSFs was not the most sensitive to absorption changes in the lower layer (Fig. 3(c)). This was also confirmed by the simulations results in Fig. 3(e). The reduced sensitivity of the late part of the TPSFs is, again, a direct consequence of the smearing effects of the IRF. The results from the two tissue-mimicking phantoms collectively demonstrate that the depth sensitivity of the TPSF can be hampered by the effects of the IRF and obtaining reliable pathlength-resolved absorption changes from the MBLL requires deconvolving TR measurements.

To illustrate the feasibility of the deconvolution approach, it was applied to series of TPSFs obtained from probes placed on the scalp of a pig during two bolus injections of ICG. Since early-arriving photons have a lower probability of probing deep tissue (in this case brain), they will mainly interrogate the superficial extra-cerebral tissue. Consequently, the time dependent changes in absorption obtained from an early time-window of the recovered DTOFs should exhibit slower kinetics due to the lower blood flow in scalp. This prediction is in agreement with the recovered $\Delta\mu_a$ curve shown in Fig. 5(a) for the early time-window. In contrast, the late-arriving photons are expected to be more sensitive to absorption changes occurring in the brain and should exhibit faster kinetics due the higher blood flow in brain. The similarity in shape of the $\Delta\mu_a$ curves acquired on the scalp and directly on the brain (Figs. 5(b) and 5(c)) confirms this prediction. These results demonstrate that the early and late parts of DTOFs measured on the scalp can be used to separate absorption changes occurring in the extra-cerebral layers from changes in the brain. One application could be to reduce scalp contributions to cerebral tissue oxygenation index measurements, which can be a significant confounder with continuous-wave NIRS [37].

A potential limitation of the method presented in this article is errors in the measured IRF and TPSFs due to timing jitter and fluctuations in the laser intensity between measurements. However, these effects can be significantly reduced by allowing sufficient time for the TR instrument to warm-up prior to data acquisition [28]. A limitation of the experimental procedure in the two-layer phantom was the necessity to replace the probes every time the absorption coefficient of the bottom layer was changed. This resulted in an erroneous downward shift in the absorption changes recovered from the two-layer phantom (red curves with triangles in Figs. 3(c) and 3(d)). This type of artefact would not happen in a clinical setting since there will be no need to replace the probes for every measurement. Another challenge when applying the deconvolution algorithm is obtaining TPSFs with sufficient signal-to-noise ratios to retrieve accurate DTOFs. In this study, noise contributions were reduced by applying wavelet denoising to the measured TPSFs and by the additional weighting constraints in the second step of the deconvolution algorithm. The stability of the deconvolution algorithm was demonstrated by its ability to characterize rapid absorption changes caused by the passage of ICG through brain. In this example, the TPSFs were acquired with an integration time of 0.4 s at a count rate of 800 kHz. A more rigorous Monte Carlo-type error analysis could be conducted to predict the relationship between experimental noise and the recovered $\Delta\mu_a$. A final consideration is the use of the MBBL, which is only appropriate for extracting $\Delta\mu_a$ if the scattering properties of the media do not change. This is generally a reasonable assumption for neuromonitoring applications since changes in hemoglobin concentration predominately affect absorption.

## 6. Conclusion

In this study, the effects of the IRF on depth-resolved absorption changes obtained using the MBBL were investigated. Absorption changes recovered from simulated and experimental TPSFs were compared to changes obtained using the corresponding DTOF data. The simulated DTOFs were generated using a finite element model while the experimental DTOFs were obtained by deconvolving the measured TPSFs and the IRF. In both cases, the results demonstrated that the instrument contribution to the measurements hampered the depth sensitivity of the TPSFs. This confounding effect could be removed by applying the MBLL to the deconvolved DTOF data, which was confirmed by the good agreement between the experimental and simulated results. The feasibility of using recovered DTOF data was shown in a pig model of the adult head. Specifically, it was shown that dynamic absorption changes recovered from the late part of the DTOFs acquired on the scalp were similar to absorption changes obtained from measurements acquired directly on the brain. These results confirm the improved depth sensitivity of DTOFs compared to raw TR measurements.

## Acknowledgments

This work was supported by the Canadian Institutes of Health Research and the Ontario Neurotrauma Foundation. We would also like to thank the animal technicians, Jennifer Hadway and Laura Morrison, for their assistance in the pig experiments.

#179884 - $15.00 USD Received 13 Nov 2012; revised 24 Jan 2013; accepted 13 Feb 2013; published 15 Feb 2013